J|A|C|S
ARTICLES
Published on Web 08/08/2002

Spectroscopic and Electronic Structure Studies of the μ_4-Sulfide Bridged Tetranuclear Cu_Z Cluster in N_2O Reductase: Molecular Insight into the Catalytic Mechanism

Peng Chen,[†] Inês Cabrito,[‡] José J. G. Moura,[‡] Isabel Moura,*[,‡] and Edward I. Solomon*[,†]

Contribution from the Department of Chemistry, Stanford University, Stanford, California 94305, and Departamento de Química, CQFB, Faculdade de Ciências e Tecnologia, Universidade Nova de Lisboa, 2825-114 Caparica, Portugal

Received April 8, 2002

Abstract: Spectroscopic methods combined with density functional calculations are used to develop a detailed bonding description of the μ_4-sulfide bridged tetranuclear Cu_Z cluster in N_2O reductase. The ground state of Cu_Z has the $1Cu^{II}/3Cu^{I}$ configuration. The single electron hole dominantly resides on one Cu atom (Cu_I) and partially delocalizes onto a second Cu atom (Cu_{II}) via a Cu_I-S-Cu_{II} σ/σ superexchange pathway which is manifested by a $Cu_{II} \rightarrow Cu_I$ intervalence transfer transition in absorption. The observed excited-state spectral features of Cu_Z are dominated by the $S \rightarrow Cu_I$ charge-transfer transitions and Cu_I based d−d transitions. The intensity pattern of individual $S \rightarrow Cu_I$ charge-transfer transitions reflects different bonding interactions of the sulfur valence orbitals with the four Cu's in the Cu_Z cluster, which are consistent with the individual Cu−S force constants obtained from a normal coordinate analysis of the Cu_Z resonance Raman frequencies and profiles. The Cu_I d orbital splitting pattern correlates with its distorted T-shaped ligand field geometry and accounts for the observed low $g_{\|}$ value of Cu_Z in EPR. The dominantly localized electronic structure description of the Cu_Z site results from interactions of Cu_{II} with the two additional Cu's of the cluster (Cu_{III}/Cu_{IV}), where the Cu−Cu electrostatic interactions lead to hole localization with no metal−metal bonding. The substrate binding edge of Cu_Z has a dominantly oxidized Cu_I and a dominantly reduced Cu_{IV}. The electronic structure description of Cu_Z provides a strategy to overcome the reaction barrier of N_2O reduction at this Cu_I/Cu_{IV} edge by simultaneous two-electron transfer to N_2O in a bridged binding mode. One electron can be donated directly from Cu_{IV} and the other from Cu_{II} through the $Cu_{II}-S-Cu_I$ σ/σ superexchange pathway. A frontier orbital scheme provides molecular insight into the catalytic mechanism of N_2O reduction by the Cu_Z cluster.

1. Introduction

Nitrous oxide reductase (N_2OR) is a multicopper containing enzyme which is the terminal oxidoreductase that catalyzes the two-electron reduction of N_2O to N_2 and water ($N_2O + 2H^+ + 2e^- \rightarrow N_2 + H_2O$, $E_0'(N_2O/N_2) = 1.35$ V) in denitrifying bacteria.[1,2] This reaction is the last step of the denitrification process ($2NO_3^- \rightarrow 2NO_2^- \rightarrow 2NO \rightarrow N_2O \rightarrow N_2$) in the global nitrogen cycle which is coupled to ATP synthesis in anaerobic respiration. This is also an important environmental process because N_2O is a greenhouse gas. The N_2O molecule is kinetically inert for thermodecomposition with a large activation barrier ($\Delta E_{act} \approx 59$ kcal/mol) even though this reaction is favored thermodynamically with a reasonable driving force ($\Delta G \approx -25$ kcal/mol).[3] Reactions of N_2O in homogeneous systems normally require transition metals as activation centers, such as Ti, V, Ni, Zr, Ru, Hf, etc.[4−9] Thus far, none of the reported metal/N_2O complexes has been structurally determined by crystallography. The N_2O in the $[(NH_3)_5Ru(N_2O)]^{2+}$ complex has been found from spectroscopy to coordinate to the Ru atom in a linear end-on mode via its terminal N atom.[10] Terminal oxygen coordination to metal sites is also implicated in the formation of the [Ru(N_2O)Ru] dimer[11,12] and spectroscopically identified in N_2O adsorption on α-Chromia.[13] Besides the N_2O reduction reaction catalyzed by N_2OR, no copper/N_2O chemistry has yet been reported.

* To whom correspondence should be addressed. E-mail: I.M., isa@dq.fct.unl.pt; E.I.S., Edward.Solomon@stanford.edu.
[†] Stanford University.
[‡] Universidade Nova de Lisboa.

(1) Zumft, W. G. *Microbiol. Mol. Biol. Rev.* **1997**, *61*, 533.
(2) Zumft, W. G.; Kroneck, P. M. H. *Adv. Inorg. Biochem.* **1996**, *11*, 1993.
(3) Jolly, W. L. *The Inorganic Chemistry of Nitrogen*; W. A. Benjamin: New York, 1964.
(4) Armor, J. N.; Taube, H. *J. Am. Chem. Soc.* **1969**, *91*, 6874.
(5) Bottomley, F.; Lin, I. J. B.; Mukaida, M. *J. Am. Chem. Soc.* **1980**, *102*, 5238.
(6) Vaughan, G. A.; Hillhouse, G. L.; Lum, R. T.; Buchwald, S. L.; Rheingold, A. L. *J. Am. Chem. Soc.* **1988**, *110*, 7215.
(7) Vaughan, G. A.; Rupert, P. B.; Hillhouse, G. L. *J. Am. Chem. Soc.* **1987**, *109*, 5538.
(8) Matsunaga, P. T.; Hillhouse, G. L. *J. Am. Chem. Soc.* **1993**, *115*, 2075.
(9) Bottomley, F.; Darkwa, J. *J. Chem. Soc., Dalton Trans. (1972−1999)* **1983**, 399.
(10) Bottomley, F.; Brooks, W. V. F. *Inorg. Chem.* **1976**, *16*, 501.
(11) Armor, J. N.; Taube, H. *Chem. Commun.* **1971**, 287.
(12) Groves, J. T.; Roman, J. S. *J. Am. Chem. Soc.* **1995**, *117*, 5594.
(13) Zecchina, A.; Cerruti, L.; Borello, E. *J. Catal.* **1972**, *25*, 55.

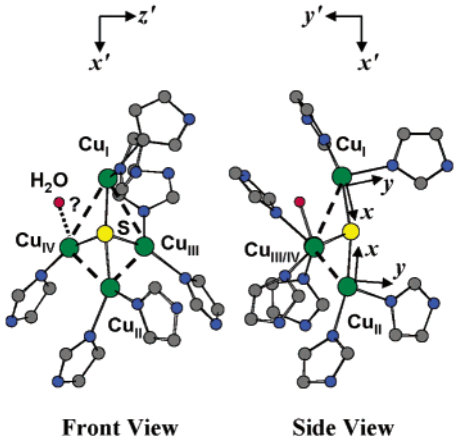

Figure 1. Crystal structure of the Cu_Z site from *Pn* (2.4 Å resolution). The Cu_4S cluster has approximate C_s symmetry with Cu_I-S-Cu_{II} defining the mirror plane. All $r(Cu-S) \approx 2.3$ Å, $r(Cu_I-Cu_{III})$ and $r(Cu_I-Cu_{IV}) \approx 3.4$ Å, $r(Cu_{II}-Cu_{III})$ and $r(Cu_{II}-Cu_{IV}) \approx 2.6$ Å, $r(Cu_{III}-Cu_{IV}) \approx 2.9$ Å. Cu_I-S-Cu_{II} angle $\approx 161°$. All other Cu−S−Cu angles are close to 90°. The water ligand is weakly bound according to the higher resolution structure of *Pd* (1.6 Å resolution) with $r(Cu_{IV}-O) \approx 2.6$ Å and $r(Cu_I-O) \approx 2.8$ Å. Molecular (primed) and local (unprimed) coordinate systems are indicated.

The crystal structure was recently solved for N_2OR from two species, *Pseudomonas nautica* (*Pn*, 2.4 Å resolution) and *Paracoccus denitrificans* (*Pd*, 1.6 Å resolution).[14,15] It is a dimeric protein. In each subunit, the C-terminal domain contains an electron-transfer Cu_A center,[16−19] and the N-terminal domain contains a Cu_Z center, which is believed to be the catalytic site.[20] The neighboring Cu_A and Cu_Z centers are from different subunits in the dimeric protein, ~10 Å away from each other, while the intrasubunit Cu_A-Cu_Z distance is ~40 Å.[14,21] The Cu_Z center has a strikingly new structural motif composed of a μ_4-sulfide bridged tetranuclear Cu cluster (Figure 1). The Cu_4S core has approximate C_s symmetry with Cu_I-S-Cu_{II} (numbering scheme for Cu's from ref 14 and given in Figure 1) defining the mirror plane. The Cu_I-S-Cu_{II} angle is ~161°. All Cu−S bond lengths are about the same, at ~2.3 Å. However, the Cu−Cu distances are very different with the lower three coppers (Cu_{II}, Cu_{III}, Cu_{IV}) closer to each other ($Cu_I-Cu_{III}/Cu_{IV} \approx 3.4$ Å, $Cu_{II}-Cu_{III}/Cu_{IV} \approx 2.6$ Å, $Cu_{III}-Cu_{IV} \approx 2.9$ Å, Figure 1). The Cu_4S core is coordinated to the protein by seven histidine ligands. Cu_I, Cu_{II}, and Cu_{III} each have two histidines, while Cu_{IV} has only one. The water ligand position is controversial between the two known structures from *Pn* and *Pd*. The higher resolution structure from *Pd* indicates it is weakly bound and located between Cu_I and Cu_{IV}.[14,15] The Cu_I/Cu_{IV} edge is the only accessible side to the Cu_4S cluster and is believed to be the substrate binding edge.[14]

Much spectroscopic data on the Cu_Z center have been published. The absorption spectrum of Cu_Z (reduced form) shows an intense band at ~640 nm giving its blue color.[20,22−25] The magnetic circular dichroism (MCD) spectrum of Cu_Z has an intense pseudo-A feature in the corresponding energy region.[20,24−26] CD, EPR, and Raman data have also been reported.[20,22,23,25,27,28] However, because of the lack of an accurate quantitation of the number of Cu atoms in the enzyme, their oxidation states, and structural information, a good understanding of these spectral features had not been accessible.[20,24]

Our initial study of the Cu_Z center used a combination of saturation magnetization, Cu K-edge XAS, Q/X-band EPR, and density functional calculations to characterize the ground state of the Cu_Z center.[29] It was determined that the Cu_Z center is an $S = {}^1/_2$ system and the Cu oxidation states are $1Cu^{II}/3Cu^{I}$. The single electron hole dominantly resides on Cu_I but is partially delocalized onto Cu_{II} via the Cu_I-S-Cu_{II} σ/σ superexchange pathway mediated by the bridging sulfide. In this study, we extend our ground-state electronic structure investigations to vibrational spectroscopy and the excited-state spectral features of the Cu_Z center. We also couple our spectroscopic studies with density functional calculations to develop a detailed description of the bonding interactions in the μ_4-sulfide bridged Cu_4S cluster, and we use this to obtain molecular insights into the catalytic mechanism of the two-electron reduction of N_2O by the Cu_Z cluster.

2. Experimental Methods

Materials. All reagents were of the highest grade commercially available and were used without further purification. *Pn* N_2OR was isolated and purified in Tris buffer (pH ≈ 7.3), as previously reported,[22] and was further exchanged to the deuterated buffer for spectroscopic studies. Enzymatic activities and copper and sulfur content were characterized as previously reported.[15,22] All studies were done at pH ≈ 7.3 unless otherwise specified. Excess dithionite solution was added to reduce the Cu_A center making it spectroscopically silent, while the oxidation state of the Cu_Z site remains unchanged.[22] From ref 22, the maximum specific activity of Pn N_2OR is achieved with preincubation of the enzyme with dithionite reduced methyl viologen, and the effect of the mediator was found to be negligible. 50% glycerol-d_3 was added as a glassing agent for low-temperature optical spectroscopy. No perturbation in the CD spectrum of Cu_Z was observed upon adding glycerol.

Spectroscopic Studies. Low-temperature absorption spectroscopy was performed on a double beam spectrophotometer (Cary 500) using a liquid helium cryostat (Janis Research Super Vari-Temp). CD/MCD data were collected on CD spectropolarimeters (JASCO J810 with a S20 PM tube for the UV/Vis region, and J200 with an InSb detector for the near-IR region) with sample compartments modified to

(14) Brown, K.; Tegoni, M.; Prudêncio, M.; Pereira, A. S.; Besson, S.; Moura, J. J.; Moura, I.; Cambillau, C. *Nat. Struct. Biol.* **2000**, *7*, 191.
(15) Brown, K.; Djinovic-Carugo, K.; Haltia, T.; Cabrito, I.; Saraste, M.; Moura, J. J. G.; Moura, I.; Tegoni, M.; Cambillau, C. *J. Biol. Chem.* **2000**, *275*, 41133.
(16) Holm, R. H.; Kennepohl, P.; Solomon, E. I. *Chem. Rev.* **1996**, *96*, 2239.
(17) Ferguson-Miller, S.; Babcock, G. T. *Chem. Rev.* **1996**, *96*, 2889.
(18) Kroneck, P. M. H.; Antholine, W. E.; Riester, J.; Zumft, W. G. *FEBS Lett.* **1989**, *248*, 212.
(19) Kroneck, P. M. H.; Antholine, W. A.; Riester, J.; Zumft, W. G. *FEBS Lett.* **1988**, *242*, 70.
(20) Farrar, J. A.; Thomson, A. J.; Cheesman, M. R.; Dooley, D. M.; Zumft, W. G. *FEBS Lett.* **1991**, *294*, 11.
(21) Rosenzweig, A. C. *Nat. Struct. Biol.* **2000**, *7*, 169.
(22) Prudêncio, M.; Pereira, A. S.; Tavares, P.; Besson, S.; Cabrito, I.; Brown, K.; Samyn, B.; Devreese, B.; VanBeeumen, J.; Rusnak, F.; Fauque, G.; Moura, J. J. G.; Tegoni, M.; Cambillau, C.; Moura, I. *Biochemistry* **2000**, *39*, 3899.
(23) Alvarez, M. L.; Ai, J. Y.; Zumft, W.; Sanders-Loehr, J.; Dooley, D. M. *J. Am. Chem. Soc.* **2001**, *123*, 576.
(24) Farrar, J. A.; Zumft, W. G.; Thomson, A. J. *Proc. Natl. Acad. Sci. U.S.A.* **1998**, *95*, 9891.
(25) Neese, F. Electronic Structure and Spectroscopy of Novel Copper Chromophores in Biology. Ph.D. Thesis, Universitat Konstanz, Konstanz, 1996.
(26) Rasmussen, T.; Berks, B. C.; Sanders-Loehr, J.; Dooley, D. M.; Zumft, W. G.; Thomson, A. J. *Biochemistry* **2000**, *39*, 12753.
(27) Dooley, D. M.; McGuirl, M. A.; Rosenzweig, A. C.; Landin, J. A.; Scott, R. A.; Zumft, W. G.; Devlin, F.; Stephens, P. J. *Inorg. Chem.* **1991**, *30*, 3006.
(28) Dooley, D. M.; Moog, R. S.; Zumft, W. G. *J. Am. Chem. Soc.* **1987**, *109*, 6730.
(29) Chen, P.; George, S. D.; Cabrito, I.; Antholine, W. E.; Moura, J. J. G.; Moura, I.; Hedman, B.; Hodgson, K. O.; Solomon, E. I. *J. Am. Chem. Soc.* **2002**, *124*, 744.

accommodate magnetocryostats (Oxford Instruments, SM4-7T). Raman spectra were obtained using a series of lines from Kr^+ (Coherent 190C-K) and Ar^+ (Coherent Sabre 25/7) ion lasers with incident power ranging from 5 to 20 mW in an ~135° backscattering configuration. Dye (Rhodamine 6G, Coherent 599) and Ti-Sapphire (Coherent 890) lasers were used for other spectral regions. Scattered light was dispersed through a triple monochromator (Spex 1877 CP, with 1200, 1800, and 2400 groove/mm gratings) and detected with a back-illuminated CCD camera (Princeton Instruments ST-135). The samples contained in NMR tubes were immersed in a liquid nitrogen finger dewar. Raman peak intensities were referenced to the ice peak at ~230 cm^{-1} for excitation profiles. Background spectra of charcoal in the same NMR tube were subtracted to remove the quartz scattering.

Normal Coordinate Analysis. Normal coordinate analyses (NCA) were performed using the QCPE program 576 by M. R. Peterson and D. F. McIntosh based on a general valence force field.[30]

DFT Calculations. Density functional calculations were performed on a PC cluster, using Gaussian 98.[31] A general basis set (6-311G* for Cu and 6-31G* for all other atoms) was used for all of the calculations. Molecular orbitals were visualized using program Molden[32] and analyzed using AOMix.[33] The structural parameters of Cu_Z were taken from the crystal structure of N_2OR (Figure 1) from *Pn* and averaged over two monomers. Metal−metal and metal−ligand bond lengths were adjusted to the more accurate values from the *Pd* N_2OR structure. The calculations are relatively insensitive to these structural modifications. Histidine ligands were modeled as NH_3. Geometry optimization of Cu−NH_3 bond lengths did not change the description of bonding. Further geometry optimization of the Cu_4S core structure will be described. Complete coordinates for calculations presented in the text are included in the Supporting Information.

rR Profile Simulations. rR excitation profiles were simulated using the time-dependent theory of electronic spectroscopy[34,35] implemented in a Mathcad script.[36] A direct modeling approach[37] was used to search for the set of excited-state parameters that produce the best simultaneous fit to the absorption band shape and rR profile data.

3. Results

3.1. Spectroscopic. Figure 2A, B, and C presents the low-temperature absorption, CD, and MCD spectra of Cu_Z. The Cu_Z absorption spectrum has an intense band at ~640 nm (~15 625 cm^{-1}, $\epsilon \approx 4000$ M^{-1} cm^{-1}), consistent with the previously reported room-temperature absorption spectrum.[20,22,23,26,27] The low-temperature absorption further resolves a number of features under this broad absorption envelope and additional electronic transitions to lower and higher energies. The MCD spectrum in Figure 2C shows an intense pseudo-A term in the 640 nm (15 625 cm^{-1}) region as previously described.[20,26] Simultaneous

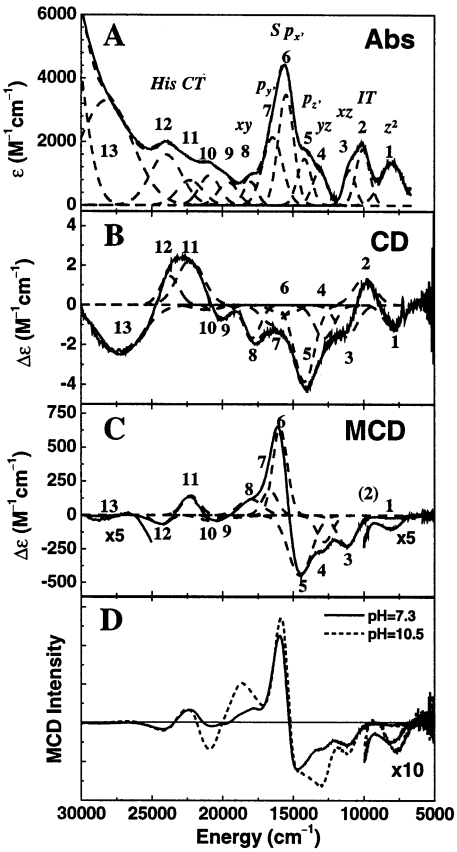

Figure 2. Optical spectra of Cu_Z (pH ≈ 7.3): (A) 10 K absorption, (B) −50 °C CD, (C) 5 K 7 T MCD, and (D) pH perturbation of MCD spectra. The MCD spectrum at pH = 9.8 is similar to the one at pH = 10.5.

Table 1. Gaussian Resolved Peak Parameters for Absorption, CD, and MCD Spectra of Cu_Z

band	assign	ν_{max} (cm^{-1})	ϵ (abs) ($M^{-1}cm^{-1}$)	$\Delta\epsilon$ (CD) ($M^{-1}cm^{-1}$)	$\Delta\epsilon$ (MCD) ($M^{-1}cm^{-1}$)	C_0/D_0[a]	Kuhn[b] ×1000
1	z^2	8015	1320	−1.1	−20	−0.016	−0.80
2	IT	10 000	1760	1.3			0.76
3	*xz*	11 140	1100	−1.6	−225	−0.218	−1.46
4	*yz*	12 900	1075	−1.7	−196	−0.194	−1.55
5	$p_{z'}$	14 300	1455	−3.9	−446	−0.327	−2.65
6	$p_{x'}$	15 675	3470	−0.5	640	0.196	−0.14
7	$p_{y'}$	16 520	2135	−1.0	182	0.091	−0.46
8	*xy*	17 980	740	−1.7	119	0.170	−2.25
9	π_1	19 775	725	−0.7	−20	−0.029	−1.03
10	π_1	20 985	930	−0.2	−39	−0.045	−0.27
11	π_1	22 270	785	2.3	143	0.193	2.87
12	π_1	24 030	1590	1.5	−71	−0.047	0.91
13	π_2	28 055	3295	−2.5	−8	−0.002	−0.76

[a] $C_0/D_0 = (kT/\beta H)(\Delta\epsilon_{MCD}/\epsilon_{abs})$. [b] Kuhn factor = $\Delta\epsilon_{CD}/\epsilon_{abs}$.

Gaussian fitting of the absorption, CD, and MCD data results in a total of 13 electronic transitions at energies lower than 30 000 cm^{-1}. (Band 7 is resolved in the resonance Raman excitation profiles, vide infra.) The spectral parameters are summarized in Table 1. Relatively large C_0/D_0 ($=(kT/\beta H) \times (\Delta\epsilon_{MCD}/\epsilon_{abs})$) ratios (~0.1−0.3) are observed for bands 3−8, indicating significant metal character in these electronic transitions.[38,39] Bands 5 and 6 form the large pseudo-A term in the

(30) McIntosh, D. F.; Michaelian, K. H.; Peterson, M. R. *Can. J. Chem.* **1978**, *56*, 1289.
(31) Frisch, M. J.; Trucks, G. W.; Schlegel, H. B.; Scuseria, G. E.; Robb, M. A.; Cheeseman, J. R.; Zakrzewski, V. G.; Montgomery, J. A., Jr.; Stratmann, R. E.; Burant, J. C.; Dapprich, S.; Millam, J. M.; Daniels, A. D.; Kudin, K. N.; Strain, M. C.; Farkas, O.; Tomasi, J.; Barone, V.; Cossi, M.; Cammi, R.; Mennucci, B.; Pomelli, C.; Adamo, C.; Clifford, S.; Ochterski, J.; Petersson, G. A.; Ayala, P. Y.; Cui, Q.; Morokuma, K.; Malick, D. K.; Rabuck, A. D.; Raghavachari, K.; Foresman, J. B.; Cioslowski, J.; Ortiz, J. V.; Baboul, A. G.; Stefanov, B. B.; Liu, G.; Liashenko, A.; Piskorz, P.; Komaromi, I.; Gomperts, R.; Martin, R. L.; Fox, D. J.; Keith, T.; Al-Laham, M. A.; Peng, C. Y.; Nanayakkara, A.; Gonzalez, C.; Challacombe, M.; Gill, P. M. W.; Johnson, B.; Chen, W.; Wong, M. W.; Andres, J. L.; Gonzalez, C.; Head-Gordon, M.; Replogle, E. S.; Pople, J. A. *Gaussian 98*, revision A.7; Gaussian, Inc.: Pittsburgh, PA, 1998.
(32) Schaftenaar, G.; Noordik, J. H. *J. Comput.-Aided Mol. Des.* **2000**, *14*, 123.
(33) Gorelsky, S. I.; Lever, A. B. P. *AOMix program*, revision 4.7; York University: Ontario, Canada, 2001.
(34) Zink, J. I.; Shin, K.-S. K. *Adv. Photochem.* **1991**, *16*, 119.
(35) Tannor, D. T.; Heller, E. J. *J. Chem. Phys.* **1982**, *77*, 202.
(36) Brunold, T. C.; Tamura, N.; Kitajima, N.; Moro-oka, Y.; Solomon, E. I. *J. Am. Chem. Soc.* **1998**, *120*, 5674.
(37) Myers, A. B.; Mathies, R. A. In *Biological Application of Raman Spectroscopy*; Spiro, T. G., Ed.; Wiley: New York, 1987; Vol. 2, p 1.
(38) Solomon, E. I.; Hanson, M. A. In *Inorganic Electronic Structure and Spectroscopy*; Solomon, E. I., Lever, A. B. P., Eds.; John Wiley & Sons: New York, 1999; Vol. 2, p 1.
(39) Band 11 is also found with a large C_0/D_0 ratio. This likely reflects the difficulty in resolving contributions from overlapping weak bands. The net C_0/D_0 ratio for bands 9−12 is low (~0.078).

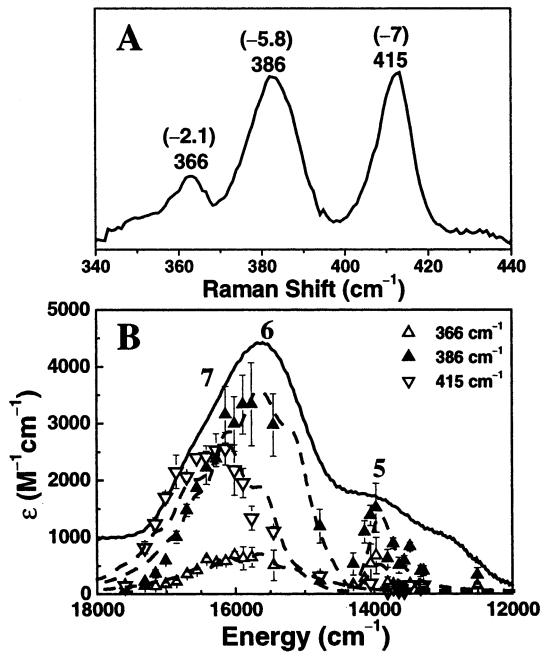

Figure 3. (A) Resonance Raman spectrum of Cu_Z excited at 624.4 nm at 77 K. Numbers in parentheses are 34-S isotope shifts (from ref 23). (B) Cu_Z rR excitation profiles overlaid on the Cu_Z absorption spectrum (solid line). Simulated profiles are in dashed lines.

MCD spectrum, and band 5 is relatively intense in the CD spectrum. Virtually no MCD intensity is observed for band 2, although it is moderately intense in the absorption spectrum.

Upon increasing the pH from 7.3 to 9.8, we observed significant perturbations of bands 1, 3, 4, 8, 9, and 10 in the MCD spectrum of Cu_Z (Figure 2D). The pK_a range (~8.5) of this deprotonation process is consistent with ionization of a water ligand bound to oxidized Cu.[16] This correlates with the fact that there is a weakly bound water near the Cu_I/Cu_{IV} edge in the Cu_Z crystal structure[14,15] and that Cu_I is the dominantly oxidized copper.[29] (The possibility of Cu_{IV} being the oxidized copper will be considered in section 3.2.) No further change is observed up to pH = 10.5, and the MCD spectrum at pH's lower than 7.3 does not change.

The resonance Raman spectrum of Cu_Z excited at 624.4 nm is presented in Figure 3A. Three dominant Raman features are observed at 415, 386, and 366 cm^{-1} with the first two peaks much stronger than the third. (The resonance Raman spectrum of Cu_Z excited at 647 nm was previously reported. It shows similar vibrational frequencies but with a different intensity pattern.[23]) All three peaks shift to lower energy upon 34-Sulfur isotope labeling.[23] On the basis of these isotope shifts and vibrational frequencies, these three features can be assigned as Cu−S based stretching vibrations.

Figure 3B gives the excitation profiles of these three vibrations overlaid on the Cu_Z absorption spectrum. All three vibrations are resonance enhanced under the strong absorption envelope centered at ~640 nm but exhibit different enhancement profiles. This leads to the resolution of three individual electronic transitions corresponding to bands 5, 6, and 7 in Figure 2. The excitation profiles of all three vibrations were simulated simultaneously with the absorption spectrum band shape using time-dependent Heller theory (a three-mode/three-state problem, Figures 3B and S1).[34,35,37] The experimentally observed sharp dip at ~14 300 cm^{-1} in the excitation profiles of the 386 and 366 cm^{-1} vibrations is found to derive from destructive interference between electronic transitions 5 and 6. The simulation parameters are summarized in Table 2.

Table 2. Excited-State Parameters from Simultaneous Fit to the rR Profiles of Cu_Z (Figure 3B) and Absorption (Figure S1)[a]

band	E_0 (cm^{-1})	Γ_r (cm^{-1})	$\Delta\nu_{366}$	$\Delta\nu_{386}$	$\Delta\nu_{415}$	μ_r^2
5	13 930	230	0.65	1.00	0.00	0.33
6	14 700	290	0.87	2.02	0.25	1.00
7	15 570	290	0.35	0.20	1.90	0.66

[a] Energies of zero-phonon transition, E_0, damping factor, Γ_r, dimensionless displacements relative to the ground state, Δ, and relative transition dipole moment, μ.

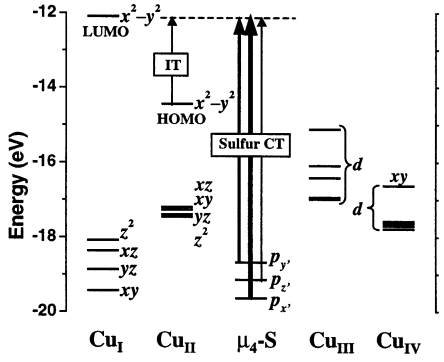

Figure 4. Energy level diagram of the spin-down set of orbitals from the B38HFP86 calculation on the Cu_Z model. Orbitals are labeled and arranged according to their main compositions from a Mulliken population analysis. Predicted electronic transitions are shown by arrows. Thicker lines represent greater intensities. Coordinate systems are as in Figure 1.

Table 3. Energies (eV) and Compositions (%) of Selected Cu 3d- and Sulfur 3p-Based Spin-Down MOs, Spin Density Distributions, and Fragment Charges from a Mulliken Population Analysis of the B38HFP86 Calculation on the Cu_Z Model

	level	E (eV)	Cu_I	Cu_{II}	Cu_{III}	Cu_{IV}	S	rest
Cu_I	x^2-y^2	−12.10	42	18	9	4	12	16
	z^2	−18.09	40	8	5	20	14	14
	xz	−18.36	57	5	6	10	13	9
	yz	−18.87	89	1	1	1	2	6
	xy	−19.43	70	2	0	1	14	13
Cu_{II}	x^2-y^2	−14.45	30	41	2	3	6	19
S	$p_{y'}$	−18.68	53	5	5	11	20	6
	$p_{z'}$	−19.15	18	9	12	10	38	13
	$p_{x'}$	−19.64	20	13	2	3	15	48
spin density			0.42	0.16	0.08	0.03	0.14	
fragment charges			1.07	0.74	0.69	0.65	−1.15	

3.2. Computational. Spin-unrestricted density functional calculations were performed to correlate with the spectroscopic results and obtain a detailed description of the electronic structure of the Cu_Z site. A spectroscopically calibrated hybrid functional is used here (38% Hartree−Fock exchange added to the BP86 functional, referred as B38HFP86).[40] Because the Cu_Z center is an $S = {}^1/_2$ system, all spin-up Cu d orbitals are occupied. The net bonding interaction involves the spin-down set, which is the focus of our analysis. Figure 4 presents the spin-down MO energy level diagram from the B38HFP86 calculation. Table 3 summarizes the energies and compositions of selected MOs. Relevant MO boundary surface plots are given in Figure 5.

The spin-down LUMO is equivalent to the singly occupied molecular orbital in a spin-restricted formalism and reflects the

(40) Szilagyi, R.; Metz, M.; Solomon, E. I. *J. Phys. Chem. A* **2002**, *106*, 2994.

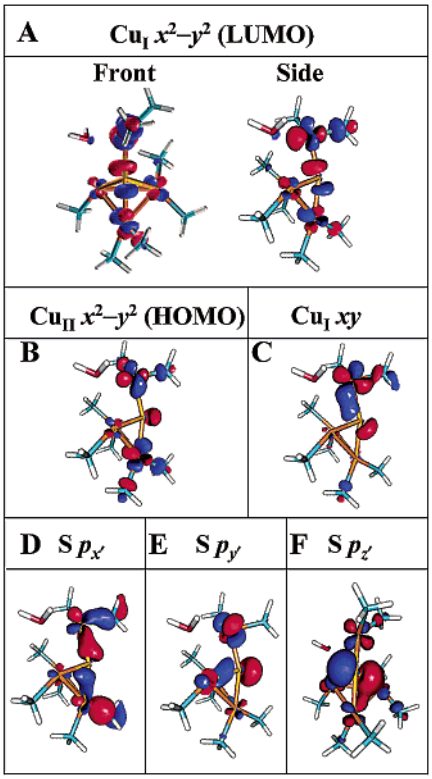

Figure 5. Boundary surface plots of selected spin-down MOs from the B38HFP86 calculation on the Cu_Z model. Note the lines connecting Cu atoms are not meant to reflect bonding interactions. Coordinate systems are defined in Figure 1.

ground state wave function and its spin distribution. The calculated ground state (Figure 5A, Table 3) is partially delocalized with Cu_I being the dominantly oxidized Cu^{II} (42% spin density, Table 3), consistent with the MCD pH perturbation results. Cu_{II} contributes 16% spin density to the ground state. The calculated spin density ratio of these two Cu's is ~5:2, which is consistent with the Q/X-band EPR results where metal hyperfine coupling to two Cu's with $A_{||}$I:$A_{||}$II ≈ 5:2 was observed.[29] There is also some spin delocalization onto Cu_{III} (8%) and Cu_{IV} (3%), whose hyperfine couplings are not resolved in the EPR spectrum but likely contribute to the overall broadening of the data. The μ_4-bridging sulfide also has significant contribution to the ground state (14% spin density). The sulfur valence orbital involved in the ground state is the S $3p_{x'}$ orbital, which forms a dominant σ-bonding interaction with the minus combination of x^2-y^2 orbitals of Cu_I and Cu_{II} (Figure 5A, see Figure 1 for definition of molecular (primed) and local (unprimed) coordinates). This σ/σ interaction constitutes an excellent superexchange pathway between Cu_I and Cu_{II} for electron delocalization. The calculation gives a large splitting between the highest singly occupied x^2-y^2 orbital and the lowest fully occupied xy orbital of Cu_I, with a calculated d orbital energy ordering of $x^2-y^2 > z^2 > xz > yz > xy$ (Figure 4, left). The calculated spin-down HOMO is the plus combination of x^2-y^2 orbitals of Cu_I and Cu_{II} and has dominant Cu_{II} x^2-y^2 orbital character (Figure 5B, Table 3). An electronic transition from this HOMO to the LUMO corresponds to an intervalence transfer (IT) transition in a class II mixed-valent center.

The calculated Cu_{IV} d manifold is low in energy, and the highest Cu_{IV} d orbital is lower than the highest d orbitals on the other three Cu atoms (Figure 4). This is consistent with Cu_{IV} having a two-coordination structure and being mostly reduced. However, the water position at the Cu_I/Cu_{IV} edge is controversial in the two Cu_Z crystal structures,[15] and its possible ligation at the Cu_{IV} site could also affect the electronic structure. To explore this structural effect, several calculations were performed where the $Cu_{IV}-OH_2$ distance was gradually shortened. The calculations show that the single electron hole still dominantly resides in the Cu_I x^2-y^2 orbital, even at a $Cu_{IV}-OH_2$ distance of ~1.9 Å (Figure S2). This is because water is not as strong of a donor ligand as histidine and amine and Cu_{IV} is only two-coordinate (not considering the possible H_2O ligand), while Cu_I is three-coordinate (Figure 1).

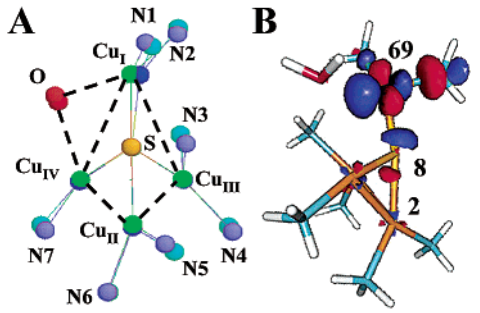

Figure 6. (A) Comparison of the crystal structure (front) of Cu_Z from *Pn* N_2OR with Cu_4S core energy optimized structure (back). (B) Boundary surface plot (side view) of the spin-down LUMO obtained from the B38HFP86 calculation on the Cu_4S core optimized structure. Overlaid numbers are the spin density distributions (%) on Cu_I, S, and Cu_{II}.

Table 4. Selected Geometry Parameter Comparison of the Cu_4S Core Optimized Structure of Cu_Z with Crystal Structures from *Pn* (2.4 Å) and *Pd* (1.6 Å)

r (Å)	opt	xtal (*Pn*)	xtal (*Pd*)
Cu_I-S	2.186	2.22	2.30
$Cu_{II}-S$	2.316	2.18	2.24
$Cu_{III}-S$	2.184	2.28	2.265
$Cu_{IV}-S$	2.138	2.06	2.29

DFT calculations using the hybrid functional B3LYP and the pure density functional BP86 were also performed. The electronic structure descriptions obtained are similar to those from the B38HFP86 calculation presented above, except that the ground-state wave function becomes more delocalized as the HF exchange contribution decreases (Figure S3). We focus on the results calculated with the B38HFP86 functional, which are in reasonable agreement with the EPR hyperfine data (vide supra).

To explore the effect of modeling the histidine ligands as amine, the $Cu-NH_3$ bond lengths in the Cu_Z model were first energy optimized, and then the Cu_4S core structure was optimized while keeping the ligand positions frozen. The optimized structure is shown in Figure 6A overlaid on the model derived from the crystal structure. Table 4 compares selected structural parameters. A detailed structure parameter comparison is given in Table S1. Overall, the optimized structure is very similar to the crystal structure. The Cu_I-S bond is shorter and the $Cu_{II}-S$ bond is longer in the geometry optimized structure than in the crystal structure. This reflects the calculated ground-state wave function (Figure 6B) for the geometry optimized structure where Cu_I is the dominantly oxidized center (69% spin density) and there is only slight delocalization onto Cu_{II} (2% spin density). The calculated short $Cu_{IV}-S$ bond results from its low coordination number. In total, these spectroscopically

derived and theoretically calculated structural features reflect a reasonable description of the Cu_Z site, although the differences among the Cu−S bonds would be exaggerated in the optimized structure due to the overestimated electronic localization on the Cu_I center (Figure 6B vs Figure 5A).

4. Analysis

4.1. Spectral Assignment: Experimental Electronic Structure. 4.1.A. S → Cu Charge-Transfer Transitions. Resonance Raman excitation profiles of Cu_Z have shown that all three Cu−S based vibrations (415, 386, and 366 cm^{-1}) are resonance enhanced under absorption bands 5, 6, and 7 (Figure 3B). These three bands are thus assigned as sulfur → Cu charge-transfer transitions, where the acceptor orbital is the σ-antibonding combination of mainly Cu_I x^2-y^2 and S $p_{x'}$ orbitals (Figure 5A, LUMO). The absorption intensity of CT transitions is mainly dependent on the ligand terms of donor/acceptor orbital overlaps.[41] Larger overlaps give more transition intensity. Band 6 is most intense in the absorption spectrum (Figure 2A) and is thus assigned as the CT transition from the S $p_{x'}$ orbital (Figure 5D), which is the σ-bonding counterpart of the LUMO acceptor orbital. This transition has the largest donor/acceptor overlap and hence should be most intense in absorption. Band 5 is the weakest in the absorption spectrum and assigned as the CT transition from the S $p_{z'}$ orbital (Figure 5F), which is out of the Cu_I x^2-y^2 orbital plane and orthogonal to this acceptor orbital. This leads to the lowest donor/acceptor overlap and the weakest absorption intensity. Band 7 is a sulfur CT transition of intermediate intensity and is assigned as the CT transition from the in-plane S $p_{y'}$ orbital (Figure 5E). Projection of the donor orbital wave functions (Figure 5D, E, and F) onto the acceptor orbital (Figure 5A) gives the same trend in the donor/acceptor orbital overlaps (ligand term) as indicated by the absorption intensity pattern, that is, large, intermediate, and low for the S $p_{x'}$, $p_{y'}$, and $p_{z'}$ CT transitions, respectively (Figure 4), although the calculated energy ordering is not the same as that experimentally observed (Figure 2).

The specific assignments of sulfur → Cu CT transitions can be used to understand the characteristic features observed in the Cu_Z CD/MCD spectra (Figure 2B and C). The CT transition out of the S $p_{z'}$ orbital (band 5) involves rotation of the S $p_{z'}$ orbital onto the S $p_{x'}$ component of the LUMO. This gives its magnetic dipole character and results in its relatively large intensity in the CD spectrum (Figure 2B, Table 1). Additionally, the bonding interaction of the S $p_{z'}$ orbital with Cu_{III}/Cu_{IV} (Figure 5F) gives this transition a nonzero transition dipole perpendicular to the Cu_I-S-Cu_{II} plane. This transition can further spin−orbit couple to the S $p_{x'}$ → Cu CT transition (band 6), which is in-plane and polarized along the S−Cu bond, leading to the large pseudo-A term observed in the MCD spectrum (Figure 2C).

The experimentally observed S → Cu CT intensity pattern gives the following bonding description: a dominant σ-bonding interaction between the μ_4-bridging sulfide and the Cu_I atom, and two additional weak orthogonal interactions involving mainly Cu_{III}/Cu_{IV} atoms in the Cu_Z cluster.

4.1.B. Ligand Field Transitions. Because only Cu_I is dominantly oxidized in the Cu_Z center,[29] four d−d transitions are expected. Bands 3, 4, and 8 can be assigned as Cu_I d−d transitions on the basis of their higher C_0/D_0 ratios (Table 1), which is due to the large spin−orbit coupling on the Cu center.[42] Band 1 is assigned as the fourth d−d transition base on its low energy. Taking the results from the B38HFP86 calculations (Figure 4, Table 3), we associated bands 1, 3, 4, and 8 with z^2, xz, yz, and xy → x^2-y^2 transitions, respectively, on the Cu_I center. The large Cu_I x^2-y^2/xy orbital splitting (Figure 2 and Table 1) comes from the ligand field geometry of the Cu_I center, which has two histidine and one sulfide ligand forming a T-shaped environment with one histidine distorted out of plane (Figure 1). The Cu_I x^2-y^2 orbital lobes are oriented directly along one of the two Cu_I-N bonds and the Cu_I-S bond, and this orbital is destabilized by the strong σ-antibonding interactions with these ligands leading to its high energy (Figure 5A). In contrast, the Cu_I xy orbital has no direct antibonding interaction and is mainly nonbonding/weak bonding in nature, resulting in its low energy (Figure 5C). The experimental Cu_I d−d manifold overlaps with the S → Cu CT bands (Figure 2), which is consistent with the results from the B38HFP86 calculation (Figure 4).

4.1.C. Intervalence Charge Transfer. The HOMO−LUMO transition in Figure 4 is predicted to be the dominant intervalence transfer (IT) transition in the B38HFP86 calculation, where the donor orbital HOMO is the plus combination of Cu_I and Cu_{II} x^2-y^2 orbitals with dominant Cu_{II} x^2-y^2 character (Figure 5B). This transition is polarized along the $Cu_{II}-Cu_I$ vector; the unidirectional nature predicts no MCD intensity. Band 2 is thus assigned to this transition as it is moderately intense in the absorption spectrum but has no discernible intensity in the MCD spectrum (Figure 2A and C). This intervalence transition reflects the coupling and electron delocalization between the Cu_I and Cu_{II} centers, which is mediated by the bridging sulfide ligand via the Cu_I-S-Cu_{II} σ/σ superexchange pathway (Figure 5A).

4.1.D. Histidine → Cu Charge Transfer. For histidines, the highest valence orbitals are π_1, π_2, and σ ring orbitals, in order of deeper binding energies.[43−45] Cu_I and Cu_{II} are the two Cu's contributing significantly to the ground state (Figure 5A), and both have two histidine ligands (Figure 1). Therefore, four histidine π_1 CT transitions are expected, and bands 9−12 are assigned as such. Bands 9 and 10 appeared to be associated with Cu_I on the basis of their pH perturbation in the MCD spectrum (Figure 2D). Bands 11 and 12 are then assigned as Cu_{II} histidine π_1 CT transitions. Band 13 is assigned as the Cu_I π_2 CT transition because it is ∼8000 cm^{-1} higher in energy than bands 9 and 10, which is the expected $\pi_1-\pi_2$ splitting for imidazole → Cu CT transitions.[43−45] These histidine CT transitions are lower in energy than that normally observed in tetragonal copper/imidazole model complexes (∼330 nm for π_1 CT transitions).[46] This is due to the low coordination number of the Cu_I and Cu_{II} centers (both three-coordinate), which decreases the energy of their d manifolds (less ligand repulsion) and thus the CT transition energies.

4.2. Vibrational Normal Modes: Cu−S Bonds. The three dominant features in the Cu_Z rR spectrum are assigned as Cu−S based stretching vibrations (Figure 3A, section 3.1). These

(41) Solomon, E. I. *Comments Inorg. Chem.* **1984**, *3*, 227.

(42) Gewirth, A. A.; Solomon, E. I. *J. Am. Chem. Soc.* **1988**, *110*, 3811.
(43) Bernarducci, E.; Schwindinger, W. F.; Hughey, J. L., IV; Krogh-Jespersen, K.; Schugar, H. J. *J. Am. Chem. Soc.* **1981**, *103*, 1686.
(44) Bernarducci, E.; Bharadwaj, P. K.; Krogh-Jespersen, K.; Potenza, J. A.; Schugar, H. J. *J. Am. Chem. Soc.* **1983**, *105*, 3860.
(45) Fawcett, T. G.; Bernarducci, E. E.; Krogh-Jespersen, K.; Schugar, H. J. *J. Am. Chem. Soc.* **1980**, *102*, 2598.
(46) Lever, A. B. P. *Inorganic Electronic Spectroscopy*, 2nd ed.; Elsevier Science: Amsterdam, The Netherlands, 1984.

vibrational modes can be understood using a Cu_4S cluster model, which has an approximate C_s symmetry with Cu_I-S-Cu_{II} defining the mirror plane (Figure 1). There are four Cu−S bonds in this cluster and thus a total of four Cu−S based stretching modes. There are two symmetric (A′ symmetry in the C_s point group) in-plane modes from $Cu_I-S/Cu_{II}-S$ vibrations and two out-of-plane modes, one the symmetric (plus) combination of $Cu_{III}-S/Cu_{IV}-S$, and the other the antisymmetric (minus, A″ symmetry) combination of $Cu_{III}-S/Cu_{IV}-S$, which should not be resonance enhanced.[47] Therefore, only three symmetric resonance Raman modes are expected, as observed experimentally (Figure 3A). The minus combination mode of $Cu_I-S/Cu_{II}-S$ should be higher in frequency than the plus combination due to the large Cu_I-S-Cu_{II} angle (∼161°), whereas the reverse case applies for the $Cu_{III}-S/Cu_{IV}-S$ vibrations because the $Cu_{III}-S-Cu_{IV}$ angle is ∼87° (Figure 1).[48,49]

To obtain a quantitative description of the Cu_Z vibrational normal modes and to determine the Cu−S bond force constants, a normal coordinate analysis (NCA) was performed on the observed vibrational data (Figure 3A), using the Cu_4S cluster model. A generalized valence force field was used. To reduce the number of the parameters, no angle bending and bond torsion modes were included. The Cu−Cu interactions were approximated and fixed to small stretching force constants calculated by Badger's rule[50,51] using the Cu−Cu force constant in the Cu_A center as a reference (k_{Cu-Cu} = 0.635 mdyn/Å at r_{Cu-Cu} = 2.47 Å).[52,53] The Cu−S stretches and their interaction force constants were allowed to float to fit the vibrational frequencies and isotope shifts (Figure 3A). It was found that the normal mode eigenvectors are dependent on the Cu−S interaction force constants and the NCA does not have a unique solution, although good agreement with the observed vibrational frequencies could be obtained. To lock onto an appropriate set of normal mode eigenvectors, excited-state nuclear distortions of the Cu_4S core were determined using the calculated eigenvectors, and the rR profile fitted S → Cu CT excited-state dimensionless displacements, Δ_n (Table 2). These were obtained from eq 1,[37]

$$\Delta r_i = 5.8065 \sum_n L_{i,n}(\Delta_n/\sqrt{\nu_n}) \qquad (1)$$

where $L_{i,n}$ is the ith element of the mass-weighted eigenvector for the nth normal mode, ν_n is the frequency (cm^{-1}) of the nth normal mode, and Δr_i (Å) is the bond length change. An iterative approach was employed to refine the calculated eigenvectors to obtain a set of nuclear distortions, which are reasonable for the specific nature of each sulfur CT excited state. The determined nuclear distortions in the excited states corresponding to bands 5, 6, and 7 (Figure 2) are given in Chart S1. The calculated force constants, vibrational frequencies, normal mode eigenvectors, and potential energy distributions (PED) are given in Table 5. The complete force field used in the NCA is given in Table S2. The four Cu_4S core stretching vibrations are visualized in the normal mode vector diagram in Figure 7.

Table 5. Observed and Calculated Vibrational Frequencies (cm^{-1}), Mass-Weighted Eigenvectors $\mathbf{L}_n$, Potential Energy Distributions (%) in Parentheses, and Selected Force Constants (mdyn/Å) from the Normal Coordinate Analysis of the Cu_4S Core[a]

exp		NCA		eigenvectors (potential energy distributions)			
^{32}S	^{34}S	^{32}S	^{34}S	$\Delta r(Cu_I-S)$	$\Delta r(Cu_{II}-S)$	$\Delta r(Cu_{III}-S)$	$\Delta r(Cu_{IV}-S)$
415	408	414.6	408.6	0.197(73)	−0.105(20)	−0.069(4)	−0.069(4)
386	380.2	386.3	379.9	0.090(29)	−0.092(29)	0.117(20)	0.117(20)
366	363.9	367.0	363.1	−0.003(0)	0.164(77)	0.085(9)	0.085(9)
		233.9	230.2	0.000(0)	0.000(0)	−0.143(48)	0.143(48)
force constants				3.29	3.11	1.31	1.31

[a] The eigenvectors and PEDs are for the ^{32}S isotopomer.

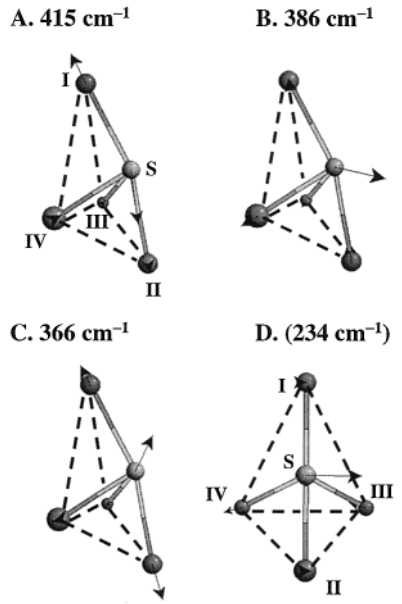

Figure 7. Vibration normal modes of the Cu_4S core of the Cu_Z site. Vector magnitudes are scaled by a factor of 10.

The calculated frequencies and isotope shifts reproduce the experimental data. The PEDs and eigenvectors indicate that the highest frequency 415 cm^{-1} mode is the minus combination of the $Cu_I-S/Cu_{II}-S$ vibration as predicted, but more localized on the Cu_I-S bond (73% Cu_I-S + 20% $Cu_{II}-S$, Table 5). The 386 cm^{-1} mode has an approximately equal mixture of Cu_I-S and $Cu_{II}-S$ stretches (29% Cu_I-S + 29% $Cu_{II}-S$), and the 366 cm^{-1} mode is dominantly the $Cu_{II}-S$ vibration (77% $Cu_{II}-S$). The unobserved antisymmetric combination of $Cu_{III}-S/Cu_{IV}-S$ vibrations is predicted to be at 234 cm^{-1} (48% $Cu_{III}-S$ + 48% $Cu_{IV}-S$), the lowest of the four Cu−S stretching normal modes. The symmetric combination of $Cu_{III}-S/Cu_{IV}-S$ is highly mixed with the Cu_I-S and $Cu_{II}-S$ stretches and is distributed mainly over the 386 cm^{-1} (40% $Cu_{III}-S/Cu_{IV}-S$) and 366 cm^{-1} (18% $Cu_{III}-S/Cu_{IV}-S$) modes. These calculated PEDs are consistent with the observed rR enhancement patterns for the 415, 386, and 366 cm^{-1} modes (Figure 3B). The absorption band 7 corresponds to the electronic excitation of S $p_{y'}$ → LUMO, where the donor orbital has a localized weak bonding interaction (Figure 5E) and the acceptor orbital has a strong antibonding interaction between the Cu_I and S atoms (Figure 5A). This would result in a mainly localized elongation along the Cu_I-S bond in the excited state, leading to the strong

(47) Czernuszewicz, R. S.; Spiro, T. G. In *Inorganic Electronic Structure and Spectroscopy*; Solomon, E. I., Lever, A. B. P., Eds.; John Wiley & Sons: New York, 1999; Vol. 1, p 353.
(48) Wing, R. M.; Callahan, K. P. *Inorg. Chem.* **1969**, *8*, 871.
(49) Sanders-Loehr, J.; Wheeler, W. D.; Shiemke, A. K.; Averill, B. A.; Loehr, T. M. *J. Am. Chem. Soc.* **1989**, *111*, 8084.
(50) Badger, R. M. *J. Chem. Phys.* **1934**, *2*, 128.
(51) Herschbach, D. R.; Laurie, V. W. *J. Chem. Phys.* **1961**, *35*, 458.
(52) Andrew, C. R.; Fraczkiewicz, R.; Czernuszewicz, R. S.; Lappalainen, P.; Saraste, M.; Sanders-Loehr, J. *J. Am. Chem. Soc.* **1996**, *118*, 10436.
(53) NCA results are relatively insensitive to the Cu−Cu force constants.

enhancement of the mainly Cu_I-S stretch based 415 cm^{-1} mode. For absorption band 6, the donor and acceptor orbitals are the bonding and antibonding combinations of the S $p_{x'}$ and Cu_I/Cu_{II} x^2-y^2 orbitals (Figure 5D and A, respectively). This excitation would result in a distortion along both Cu_I-S and $Cu_{II}-S$ bonds in the excited state, giving strong enhancement to the $Cu_I-S/Cu_{II}-S$ based 386 cm^{-1} mode. The absorption band 5 corresponds to an electronic excitation from the S $p_{z'}$ orbital, which is σ-bonding to Cu_{III} and Cu_{IV} (Figure 5F), to the LUMO, which is antibonding in terms of $Cu_{III}/Cu_{IV}-S$ interactions (Figure 5A). This excitation would lead to the elongation of the $Cu_{III}-S$ and $Cu_{IV}-S$ bonds in the excited state, which would give resonance enhancement to the $Cu_{III}-S/Cu_{IV}-S$ based vibrations. The 386 cm^{-1} mode has more $Cu_{III}-S/Cu_{IV}-S$ character (40%) and thus is more enhanced under absorption band 5. In contrast, the 415 cm^{-1} mode has little $Cu_{III}-S/Cu_{IV}-S$ character (8%, Table 5), and little enhancement is observed for this vibration under absorption band 5.

The calculated force constants are $k(Cu_I-S) = 3.29$ mdyn/Å, $k(Cu_{II}-S) = 3.11$ mdyn/Å, and $k(Cu_{III}-S) = k(Cu_{IV}-S) = 1.31$ mdyn/Å (Table 5). This is consistent with the electronic structure of the Cu_Z site, where the bridging sulfide forms a strong σ-interaction with the dominantly oxidized Cu_I and mediates a σ/σ superexchange pathway to the Cu_{II}, giving it some oxidized character. Cu_{III} and Cu_{IV} are dominantly reduced which leads to the weak $Cu_{III}-S$ and $Cu_{IV}-S$ bonds.

4.3. EPR *g*-Values: Ligand Field versus Delocalization. One unique spectral feature of the Cu_Z site is the extremely low $g_{||}$ value (=2.16) observed in the EPR,[29] in contrast to the $g_{||} \approx 2.2-2.3$ for normal Cu^{II} complexes.[41] This could be due to a highly covalent Cu−S bond where the spin delocalization onto ligands would reduce the metal character in the ground state and thus the $g_{||}$ value.[38,54] However, the B38HFP86 calculation indicates there is only 14% sulfur character in the ground state (Table 3, section 3.2);[55] the Cu−S bond is thus not very covalent, and this cannot account for the low $g_{||}$ value.

Because the Cu_Z site is a partially delocalized class II mixed-valent system with Cu_I and Cu_{II} being the main contributing Cu centers,[29] the system **g** tensor is a delocalization weighted sum of the local **g** tensors for the monomeric sites[56,57] and is affected by the extent of delocalization and the noncollinearity of the local **g** tensors which are determined by the local ligand field geometry around each Cu atom. The system *g*-values can be determined using local **g** tensors constructed from the local ligand field geometry of Cu_I and Cu_{II} (Figure 8A) by diagonalizing the $\mathbf{g}^{sys}$ tensor obtained from eq 2[57]

$$\mathbf{g}^{sys} = \alpha^2\mathbf{g}^A + (1-\alpha^2)\mathbf{T}\mathbf{g}^B\mathbf{T}^T \qquad (2)$$

where the α^2 is the mixed-valent delocalization parameter ($\alpha^2 = 0.5$ for complete delocalization),[58,59] $\mathbf{g}^{A,B}$ are the local **g** tensors, and $\mathbf{T}(\alpha',\beta',\gamma')$ is the Euler angle rotation matrix from tensor $\mathbf{g}^B$ to $\mathbf{g}^A$ ($\alpha' = \gamma' = 0$, $\beta' = 22°$, Figure 8A). Typical tetragonal *g*-values ($g_x = g_y = 2.04$, $g_z = 2.25$) were used for the $\mathbf{g}^{A,B}$ tensors.[38,60] Figure 8B gives the calculated dependence

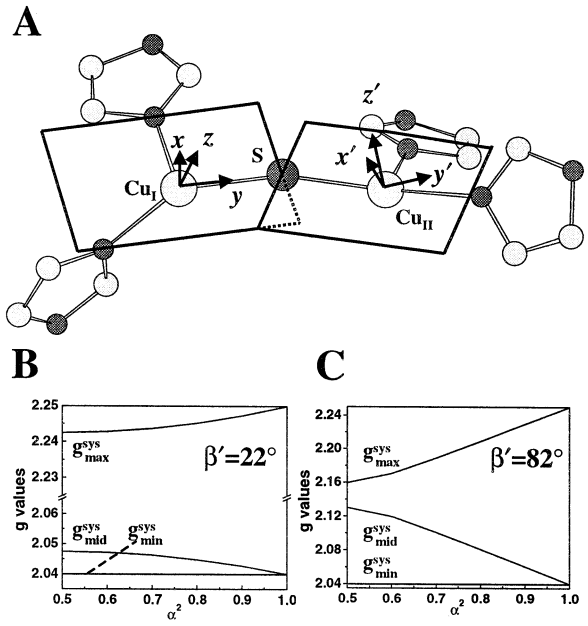

Figure 8. Cu_I-Cu_{II} dimer **g** tensor. (A) Local **g** tensor construction on Cu_I and Cu_{II} sites based on their ligand field geometries. The *z* (*z*′) direction is perpendicular to the ligand field equatorial plane defined by the sulfide and histidine ligands, *y* (*y*′) directions on both Cu's are defined parallel to each other, and $x = y \times z$. The Euler angles thus defined are $\alpha' = \gamma' = 0$ and $\beta' \approx 22°$, where β' is the tilting angle of *z* and *z*′ with respect to each other. Note the local **g** tensor orientations are different from those in Figure 1 to simplify the Euler angles. (B) Calculated *g*-value dependence on α^2 at $\beta' = 22°$. (C) Calculated *g*-value dependence on α^2 assuming $\beta' = 82°$.

of the system *g*-values on the delocalization parameter α^2. At $\beta' = 22°$, the system *g*-values do not vary much and are close to axial ($g_{min} \approx 2.04$, $g_{mid} \approx 2.05$, and $g_{max} \approx 2.24$) even at the complete delocalization limit ($\alpha^2 = 0.5$). Only when the two local **g** tensors are close to orthogonal ($\alpha^2 = 0.5$, Figure 8C, left) could g_{max} reduce to 2.16, and this leads to a rhombic (close to inverse) EPR pattern, which is not experimentally observed.[29] Therefore, spin delocalization does not appear to be responsible for the low $g_{||}$ value of Cu_Z.

From ligand field theory, the $g_{||}$ value of Cu^{II} EPR is inversely proportional to the $xy \rightarrow x^2-y^2$ transition energy, and a high-energy *xy* excited state could also contribute to the low $g_{||}$ value observed for Cu_Z.[54] Taking D_{4h} $CuCl_4^{2-}$ as a reference, as it has metal character in the ground state (63% Cu)[41] similar to that calculated by DFT for Cu_Z (69% total Cu, Table 3), the $g_{||}$ value of Cu_Z could be estimated from the relative energies of the $xy \rightarrow x^2-y^2$ transition (eq 3)

$$\Delta g_{||}(Cu_Z) = \frac{E_{xy}(CuCl_4^{2-})}{E_{xy}(Cu_Z)}\Delta g_{||}(CuCl_4^{2-}) \qquad (3)$$

where $\Delta g_{||}$ is the deviation of $g_{||}$ from the spin-only value (2.0023), and E_{xy} is the $xy \rightarrow x^2-y^2$ transition energy (for D_{4h} $CuCl_4^{2-}$, $g_{||} \approx 2.22$, $E_{xy} = 12\,500$ cm^{-1}).[41,61] The E_{xy} for Cu_Z from abs/CD/MCD is ~17 980 cm^{-1} (Table 1), which gives $g_{||} \approx 2.16$, consistent with experiment. Therefore, the low $g_{||}$ value

(54) McGarvey, B. R. In *Transition Metal Chemistry*; Carlin, R. L., Ed.; Marcel Dekker: New York, 1966; Vol. 3, p 89.
(55) Preliminary Cu_Z sulfur K-edge data are consistent with this S-covalency. George, S. D.; Solomon, E. I., unpublished results.
(56) Westmoreland, T. D.; Wilcox, D. E.; Baldwin, M. J.; Mims, W. B.; Solomon, E. I. *J. Am. Chem. Soc.* **1989**, *111*, 6106.
(57) Neese, F.; Zumft, W. G.; Antholine, W. E.; Kroneck, P. M. H. *J. Am. Chem. Soc.* **1996**, *118*, 8692.
(58) Hush, N. S. *Prog. Inorg. Chem.* **1967**, *8*, 391.
(59) Robin, M. B.; Day, P. *Adv. Inorg. Chem. Radiochem.* **1967**, *10*, 247.
(60) $g_{||}$ values ranging from 2.2 to 2.35 and $g_\perp$ values ranging from 2.02 to 2.06 for the local monomeric **g** tensors were investigated. All results are similar to those presented here.
(61) Hitchman, M. A.; Cassidy, P. J. *Inorg. Chem.* **1979**, *18*, 1745.

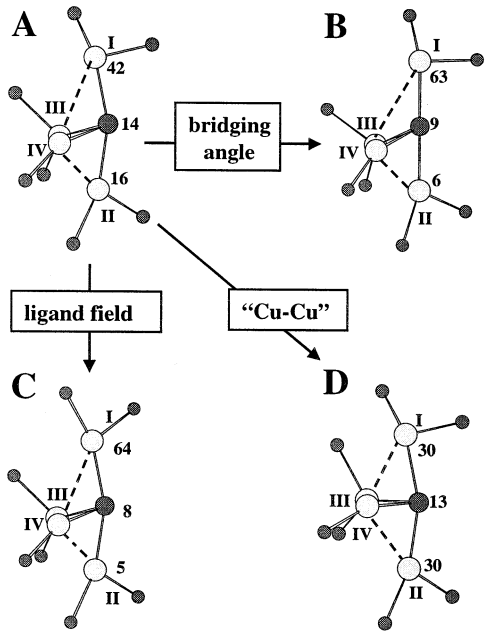

Figure 9. Structurally perturbed models of the Cu_Z site. Water ligand is not shown for clarity. B38HFP86 calculated spin density distributions (%) are given for Cu_I, S, and Cu_{II}. (A) Crystal structure derived model. (B) Linear Cu_I-S-Cu_{II} bridging angle. (C) Cu_I/Cu_{II} ligand fields symmetrized (ligand field of Cu_I modified to that of Cu_{II}. (D) $Cu_{II}-Cu_{III}/Cu_{IV}$ interaction eliminated by moving Cu_{III}/Cu_{IV} away from Cu_{II} to bisect the Cu_I-S-Cu_{II} angle ($Cu_I-Cu_{III/IV} \approx Cu_{II}-Cu_{III/IV} \approx 3$ Å).

of Cu_Z appears to reflect the high $xy \rightarrow x^2-y^2$ ligand field transition energy, which derives from the specific ligand field geometry of Cu_I (Figure 1, section 4.1.B).

4.4. Structural Perturbations: Geometric Contribution to Electronic Structure. The Cu_Z center is a class II mixed-valent site with the single hole dominantly localized on Cu_I and partially delocalized onto Cu_{II} via the Cu_I-S-Cu_{II} superexchange pathway. To understand the geometric contribution to electronic localization/delocalization, three perturbations on the crystal structure derived Cu_Z model (Figure 9A) were evaluated by electronic structure calculations. (1) The Cu_I-S-Cu_{II} bridging angle was made linear (Figure 9B). (2) The Cu_I/Cu_{II} ligand fields were symmetrized (Figure 9C). (3) Possible $Cu_{II}-Cu_{III}/Cu_{IV}$ interactions were eliminated by moving Cu_{III}/Cu_{IV} away from Cu_{II} so that the $Cu_{III}-S-Cu_{IV}$ plane bisects the Cu_I-S-Cu_{II} angle (Figure 9D). The DFT calculated ground-state spin density distributions indicate that the linear Cu_I-S-Cu_{II} angle and the symmetrized Cu_I/Cu_{II} ligand fields, in fact, both resulted in a more localized ground state on the Cu_I atom (63% and 64% Cu_I spin density, respectively, Figure 9B and C) than that of the crystal structure derived model (42% Cu_I spin density, Figure 9A). This increased localization derives from the decreased bridging sulfide covalency in the ground-state wave function [9% (Cu_I-S-Cu_{II} linear model) and 8% sulfide (ligand fields symmetrized model) vs 14% (crystal structure model), see Figure 9B and C vs Figure 9A], which leads to less superexchange and thus more localization.[62] In contrast, moving the Cu_{III}/Cu_{IV} centers away from Cu_{II} resulted in a completely delocalized ground state (30% Cu_I and 30% Cu_{II} spin density, Figure 9D), even though a slight decrease in the bridging sulfide covalency is observed (14% → 13% S character). This demonstrates that there is some interaction between Cu_{II} and the Cu_{III}/Cu_{IV} pair in the lower trinuclear unit of the Cu_Z center due to their close proximity that leads to the dominantly localized (or partially delocalized) electronic structure description of the Cu_Z center. The nature of this interaction is discussed below.

5. Discussion

5.1. Bonding Description of the μ_4-Sulfide Bridged Tetranuclear Cu_Z Cluster. A combination of spectroscopic techniques and density functional calculations has provided a detailed bonding description of the μ_4-sulfide bridged tetranuclear Cu_Z center. The ground state of Cu_Z has the $1Cu^{II}/3Cu^{I}$ configuration and is a class II mixed-valent system.[29] The single hole dominantly resides on Cu_I which has a distorted T-shaped three-coordinate ligand field resulting in the low His → Cu CT transition energies, and the large splitting of the x^2-y^2 and the xy orbital leading to the low $g_{||}$ value observed in EPR (sections 4.1 and 4.3). The bridging sulfide $p_{x'}$ valence orbital is oriented along the Cu_I-S-Cu_{II} direction and forms a dominant σ-interaction with the Cu_I x^2-y^2 orbital leading to the strong S → Cu CT transition in the absorption spectrum (section 4.1). The same sulfur $p_{x'}$ orbital also has good σ interaction with the Cu_{II} x^2-y^2 orbital, forming a Cu_I-S-Cu_{II} σ/σ superexchange pathway for electron delocalization from Cu_I to Cu_{II}, which is manifested in the absorption spectrum by a $Cu_{II} \rightarrow Cu_I$ intervalence transfer transition (section 4.1). The S $p_{z'}$ valence orbital (perpendicular to the Cu_I-S-Cu_{II} plane) has a weak bonding interaction with Cu_{III} and Cu_{IV}, which gives a nonzero dipole moment to the S $p_{z'} \rightarrow$ Cu CT transition perpendicular to the S $p_{x'} \rightarrow$ Cu CT transition, resulting in an intense pseudo-A term in the MCD spectrum. The S $p_{y'}$ valence orbital is in the Cu_I-S-Cu_{II} plane and gives rise to a CT transition with intermediate intensity in absorption (section 4.1). The spectroscopically determined μ_4-sulfide bonding interactions with the four Cu's in the Cu_Z cluster are consistent with the individual Cu−S bond strengths from the stretching force constants determined from the normal coordinate analysis of rR vibrational data, with $k(Cu_I-S) > k(Cu_{II}-S) > k(Cu_{III}-S) \approx k(Cu_{IV}-S)$ (section 4.2).

The geometric origin of the dominantly localized (or partially delocalized) electronic structure description of the Cu_Z center is the asymmetry of Cu−Cu distances in the Cu_4S cluster, where the short distances between Cu_{II} and Cu_{III}/Cu_{IV} provide an interaction leading to the hole localization on Cu_I (section 4.4). This interaction between Cu_{II} and Cu_{III}/Cu_{IV} could be due to direct Cu−Cu bonding, or an electrostatic effect due to the positive charge on Cu_{III}/Cu_{IV} which can trap electron density on Cu_{II} (i.e., hole localization on Cu_I). Because Cu_{II}, Cu_{III}, and Cu_{IV} are all dominantly reduced with closed-shell d^{10} electron configurations, any direct Cu^I-Cu^I bonding interaction must involve copper 4s/4p mixing. So far, no spectroscopic evidence for the presence of any Cu^I-Cu^I bond has been reported.[63] MO calculated Cu−Cu overlap populations for several representative Cu^I binuclear and cluster systems were analyzed for bonding interactions.[64,65] "The results are that direct Cu^I-Cu^I bonding

(62) Glaser, T.; Rose, K.; Shadle, S. E.; Hedman, B.; Hodgson, K. E.; Solomon, E. I. *J. Am. Chem. Soc.* **2001**, *123*, 442.

(63) Koten, G. V.; James, S. L.; Jastrzebski, J. T. B. H. In *Comprehensive Organometallic Chemistry II. A Review of the Literature 1982−1994*; Wardell, J. L., Ed.; Elsevier Science, Inc.: New York, 1995; Vol. 3, p 57.

(64) Mehrotra, P. K.; Hoffmann, R. *Inorg. Chem.* **1978**, *17*, 2187.

Table 6. DFT Calculated Cu−Cu Overlap Populations (Electron)

	Cu_Z model		Cu_2^{2+} model	
	r_{Cu-Cu}(Å)	overlap	r_{Cu-Cu}(Å)	overlap
$Cu_{II}-Cu_{III}$	2.57	0.0114	2.58	0.0283
$Cu_{II}-Cu_{IV}$	2.58	0.0076	2.78	0.0175
$Cu_{III}-Cu_{IV}$	2.93	0.0073	2.98	0.0100
Cu_I-Cu_{III}	3.36	−0.0213	3.18	0.0055
Cu_I-Cu_{IV}	3.38	−0.0155		

is at best weak, and possibly negligible."[66] The Cu−Cu overlap populations for the Cu_Z model from the B38HFP86 calculations were analyzed and compared to the simple Cu_2^{2+} model system, the best case where a weak Cu^I-Cu^I bond was suggested from the small positive overlap population (Table 6).[64] The largest overlap population is for the $Cu_{II}-Cu_{III}$ pair in Cu_Z, but the magnitude is only $\sim 1/3$ of that in the Cu_2^{2+} model at a similar Cu−Cu distance (Table 6). Therefore, there is virtually no direct metal−metal bonding in the reduced $Cu_{II}Cu_{III}Cu_{IV}$ unit. To evaluate the electrostatic effect from Cu_{III}/Cu_{IV} on the Cu_I-S-Cu_{II} localization, a simplified model was constructed with symmetrized ligand fields on both Cu_I and Cu_{II}, while Cu_{III} and Cu_{IV} were substituted by positive point charges (with the Mulliken charges obtained for Cu_{III} and Cu_{IV} from the Cu_Z calculation, Figure S4). When the point charges are located halfway between Cu_I and Cu_{II}, a delocalized ground state is obtained (Figure S4A, symmetric model), while the asymmetric model resulted in a localized ground state (Figure S4B, asymmetric model). This indicates that the interaction between Cu_{II} and the Cu_{III}/Cu_{IV} pair is mainly electrostatic, where the positive charges on Cu_{III}/Cu_{IV} trap electron density on Cu_{II} (hole on Cu_I) and result in the dominantly localized (or partially delocalized) electronic structure description of Cu_Z.

Structural perturbation similar to that in Figure 9D (section 4.4) was also performed on the Cu_4S core optimized structure (section 3.2, Figure 6) by moving Cu_{III}/Cu_{IV} away from Cu_{II}. The total energy of the model went up by ~4 kcal/mol even after re-optimizing the Cu_4S core while keeping the ligands in the perturbed state (data not shown). This indicates that the asymmetry of Cu−Cu distances in the Cu_Z cluster in the crystal structure is consistent with the total energy preference of the Cu_4S core rather than restricted by the protein.

5.2. Electronic Structure Contributions to Reactivity. The enzyme N_2OR catalyzes the two-electron reduction of N_2O to N_2 and H_2O at the Cu_Z center, which involves the cleavage of the N_2-O bond and the reduction of the O atom to the oxide level. In the gas phase, the N_2-O cleavage generates N_2 and a triplet O atom (^3P) in the first elementary step, which is energetically uphill ($\Delta H \approx 40$ kcal/mol) and has a high reaction barrier due to the spin change. This leads to the high activation energy for the full thermodecomposition reaction of N_2O ($\Delta E_{act} \approx 59$ kcal/mol), despite its thermodynamic driving force ($\Delta G \approx -29$ kcal/mol).[3] In N_2O model chemistry, transition metals are used as activation centers to overcome this reaction barrier by donating two electrons to N_2O. The two electrons can come either from a single metal center (e.g., Ru, Ti, V)[12,67] or from two metal centers forming dimeric products (e.g., Ti, V).[5,9,68] Two electrons can also come from coordinated ligands if no electrons are available from the metal center (e.g., Hf, Zr, Ti, Ni).[6−8,69] With few exceptions,[8] high-valent metal-oxo bonds are normally formed in the products, which stabilize the oxide formed and drive the reaction.

The spectroscopically calibrated MO energy level diagram of Cu_Z (Figure 4) indicates that the bridging sulfide and amine (histidine) ligand orbitals are deep in energy, and the high-energy occupied MOs are the Cu d orbitals. Therefore, the redox reaction with the N_2O substrate should mainly involve the oxidation of Cu atoms in the cluster (i.e., Cu_{II}, Cu_{III}, or Cu_{IV}, because Cu_I is dominantly oxidized and further oxidation would lead to Cu^{III} which is not established in biological Cu systems). The substrate binding edge of the Cu_Z cluster has one dominantly oxidized Cu_I, one dominantly reduced Cu_{IV}, and an exchangeable water ligand (weakly bound). Both Cu_I and Cu_{IV} are coordinately unsaturated with open coordination positions oriented toward the exchangeable water. The Cu_I-Cu_{IV} distance is ~3.4 Å (Figure 1), which is in the range for μ-1,3- or μ-1,1-N_2O bridging, as is widely observed in isoelectronic azide-Cu_2 complexes.[70−73] This possible bridging interaction of N_2O at the Cu_I/Cu_{IV} edge provides a mechanism for overcoming the reaction barrier by simultaneous two-electron reduction of N_2O at the Cu_Z site. One electron can be donated directly from Cu_{IV} and the other from Cu_{II} through the $Cu_{II}-S-Cu_I$ σ/σ superexchange pathway.

The frontier molecular orbital (FMO)[74,75] concept can be used to obtain electronic structure insight into the simultaneous two-electron-transfer pathway from Cu_Z to N_2O. In the FMO theory, the redox active molecular orbitals are the lowest unoccupied MOs of the electron acceptor and the highest occupied MOs of the electron donor. These MOs are the main participants in the redox reaction, and the donor/acceptor orbital overlaps dominate the reaction pathway. The LUMO of the N_2O molecule is a π orbital with dominantly terminal N character (Scheme 1A, Figure S6) and is the electron acceptor orbital for its reduction. On the Cu_I/Cu_{IV} substrate binding edge of Cu_Z, the highest occupied MOs (HOMOs) are the Cu_Z HOMO (Figures 4 and 5B), which is the Cu_{II} x^2-y^2 orbital with significant Cu_I x^2-y^2 character from superexchange mediated electron delocalization, and the highest occupied Cu_{IV} xy orbital (Figures 4 and S5). These two MOs can serve as the electron donors for the two-electron reduction of N_2O.[76] For the μ-1,1-N_2O bridging mode possibility, terminal nitrogen coordination configuration is least likely due to the difficulty in oxo-transfer, while terminal μ-1,1 oxygen coordination has unfavorable N_2O/Cu_Z LUMO/HOMO overlap due to the small oxygen contribution in the N_2O LUMO (Scheme 1A and B, Figure S6). For the μ-1,3-N_2O bridging mode, the LUMO of N_2O has good overlap with both the Cu_{IV} xy orbital and the Cu_{II} x^2-y^2 orbital (through its Cu_I x^2-y^2

(65) Avdeef, A.; Fackler, J. P., Jr. *Inorg. Chem.* **1978**, *17*, 2182.
(66) Cotton, F. A.; Wilkinson, G. *Advanced Inorganic Chemistry, A Comprehensive Text*, 4th ed.; John Wiley & Sons: New York, 1980.
(67) Smith, M. R., III; Matsunaga, P. T.; Anderson, R. A. *J. Am. Chem. Soc.* **1993**, *115*, 7049.
(68) Bottomley, F.; Lin, I. J. B.; White, P. S. *J. Am. Chem. Soc.* **1981**, *103*, 703.
(69) Vaughan, G. A.; Sofield, C. D.; Hillhouse, G. L. *J. Am. Chem. Soc.* **1989**, *111*, 5491.
(70) Drew, M. G. B.; McCann, M.; Nelson, S. M. *J. Chem. Soc., Chem. Commun.* **1979**, 481.
(71) Comarmond, J.; Plumeré, P.; Lehn, J.-M.; Agnus, Y.; Louis, R.; Weiss, R.; Kahn, O.; Morgenstern-Badarau, I. *J. Am. Chem. Soc.* **1982**, *104*, 6330.
(72) Agnus, Y.; Louis, R.; Weiss, R. *J. Am. Chem. Soc.* **1979**, *101*, 3381.
(73) Sikorav, S.; Bkouche-Waksman, I.; Kahn, O. *J. Am. Chem. Soc.* **1984**, *106*, 490.
(74) Klopman, G. *J. Am. Chem. Soc.* **1968**, *90*, 223.
(75) Salem, L. *J. Am. Chem. Soc.* **1968**, *90*, 543.
(76) Note the Cu_{III} d orbitals are not accessible from the substrate binding side.

Scheme 1. FMO Interactions between N_2O and Cu_Z[a]

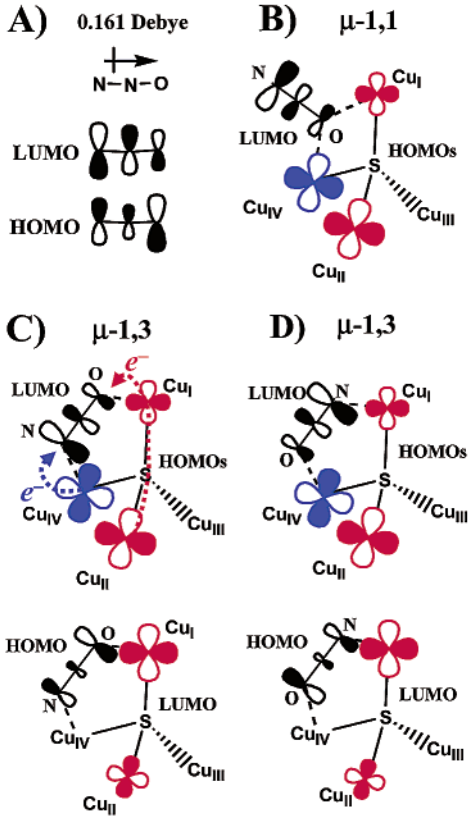

[a] Bridging sulfide contributions in the MOs are not shown.

delocalized component) in both orientations (Scheme 1C and D), which is favorable for electron transfer from Cu_Z to N_2O. The configuration with oxygen coordinating to Cu_I in the μ-1,3 bridging mode has an additional favorable N_2O/Cu_Z HOMO/LUMO interaction (Scheme 1C, lower), where the dominant oxygen character of the N_2O HOMO (Scheme 1A and Figure S6) has good overlap with the Cu_Z LUMO, which is dominantly a Cu_I x^2-y^2 orbital (Figure 5A). This N_2O/Cu_Z HOMO/LUMO interaction would contribute to the N_2O binding affinity at the Cu_I/Cu_{IV} edge of the Cu_Z cluster. Moreover, the μ-1,3 bridging mode with oxygen on Cu_I has the favorable electrostatic interaction because this is the dominantly oxidized copper (for N_2O, dipole moment = 0.161 D[77]).

(77) *CRC Handbook of Chemistry and Physics*, 76th ed.; Lide, D. R., Ed.; CRC Press: New York, 1996.

In summary, the μ_4-sulfide bridged tetranuclear Cu_Z center of N_2OR provides a strategy to overcome the reaction barrier of N_2O reduction by simultaneous two-electron transfer. One electron can be donated directly from Cu_{IV} and the other from Cu_{II} through the $Cu_{II}-S-Cu_I$ σ/σ superexchange pathway (Scheme 1C, upper). The HOMOs on the Cu_I/Cu_{IV} edge have favorable overlaps with the N_2O LUMO in the μ-1,3 bridging mode, while the additional N_2O/Cu_Z HOMO/LUMO interaction (oxygen on Cu_I) and electrostatic effect with Cu_I further facilitate the N_2O binding. Possible H-bonding interaction of the coordinated oxygen atom to the backbone NH group of His376 (estimated $r_{O-N} \approx 3.0$ Å)[14] and/or additional oxygen$-Cu_{IV}$ interaction (estimated $r_{O-CuIV} \approx 3.5$ Å) during the reaction leading to oxo-bridging between Cu_I and Cu_{IV} would further stabilize the product facilitating the reaction.[78] After the N_2O reduction, the two-electron oxidized Cu_Z center would have the two additional electron holes on Cu_{II} and Cu_{IV}, which are in the lower trinuclear $Cu_{II}Cu_{III}Cu_{IV}$ component of the cluster. The proximity of Cu_{II}, Cu_{III}, and Cu_{IV} atoms could result in the electron delocalization over this trinuclear unit contributing to the stabilization of the oxidized state of the Cu_Z center and thus the N_2O reduction. Finally, good electron-transfer pathways from the bridging thiolates and one histidine ligand of the neighboring Cu_A center in the dimeric protein to the Cu_{II} and Cu_{IV} atoms of the tetranuclear cluster would allow rapid re-reduction of the Cu_Z site during turnover.[29]

Acknowledgment. We thank Dr. Serena D. George for useful discussions. This research is supported by NIH DK-31450 (E.I.S.) and PRAXIS (J.J.G.M. and I.M.). P.C. is a Gerhard Casper Stanford Graduate Fellow. I.C. has a PRAXIS-BD fellowship.

Supporting Information Available: Model coordinates used for the calculations, detailed geometric comparison of the Cu_4S core optimized structure and crystal structures, complete NCA force fields, additional Heller theory fitting results, and DFT calculated energy level diagrams and wave functions (PDF). This material is available free of charge via the Internet at http://pubs.acs.org.

JA0205028

(78) Note the protonation of the coordinated oxygen atom of N_2O during N_2-O bond cleavage is not considered due to the very small dipole moment of N_2O (0.161 D).